



# Synergistic surface activation during photocatalysis on perovskite derivative sites in heterojunction

Yalin Yang<sup>a</sup>, Zheyang Chen<sup>a</sup>, Hanlin Huang<sup>a,\*</sup>, Yuxin Liu<sup>b</sup>, Junhua Zou<sup>c</sup>, Shuqi Shen<sup>a</sup>,  
Jiawei Yan<sup>a</sup>, Jinshui Zhang<sup>c</sup>, Zanyong Zhuang<sup>a</sup>, Zhongzhen Luo<sup>a</sup>, Chengkai Yang<sup>a,\*</sup>, Yan Yu<sup>a,\*</sup>,  
Zhigang Zou<sup>a,d,\*</sup>

<sup>a</sup> Key Laboratory of Eco-materials Advanced Technology, College of Materials Science and Engineering, Fuzhou University, Fuzhou 350108, China

<sup>b</sup> Department of Biomolecular System, Max-Planck Institute of Colloids and Interfaces, Am Muehlenberg 1, Potsdam 14476, Germany

<sup>c</sup> State Key Laboratory of Photocatalysis on Energy and Environment, College of Chemistry, Fuzhou University, Fuzhou 350108, China

<sup>d</sup> Eco-materials and Renewable Energy Research Center (ERERC), National Laboratory of Solid State Microstructures and Department of Physics, Nanjing University, Nanjing 210093, China

## ARTICLE INFO

### Keywords:

Perovskite

Heterojunction

Surface activation

C-H conversion

Photocatalysis

## ABSTRACT

Halide perovskites and derivatives have been used as emerging photocatalysts due to their unique optoelectronic and structural diversity. However, compared with the well-explored photophysical processes for light-driven more energetic carriers to trigger redox reactions, catalytic effects on the surface of halide perovskite or their derivatives for chemical transformations between reactive species are seldom addressed, which is equally important for improving the efficiency for halide perovskite-based photocatalysts. Here, we demonstrate that Cs<sub>3</sub>Bi<sub>2</sub>Br<sub>9</sub> sites in the Cs<sub>3</sub>Bi<sub>2</sub>Br<sub>9</sub>/CdS heterojunction, not only participate in light-driven processes, but also play a vital role for the activation and conversion of key intermediates during C(sp<sup>3</sup>)-H bond transformation, via a more thermodynamically and kinetically favorable surface reaction pathway. Besides, various aromatic hydrocarbons can be effectively photocatalytically converted to corresponding aldehydes/ketones as major products. This work highlights the importance of surface catalysis mechanism in photocatalysis not only for halide perovskites but also for other semiconductors.

## 1. Introduction

Photocatalysis is capable of driving challenging redox reactions utilizing photons as effective activators under mild conditions [1–4]. The efficiency of light excitation, charge separation and surface reaction, which are three fundamental and key processes during photocatalytic transformations, determines the overall performance [5–10]. To address these crucial issues, in the last few decades, efforts have been devoted to developing photocatalysts with strong photon absorption across the spectrum [11,12], efficient transfer of photo-induced carriers [13,14], and rapid reaction rates on the surface [15,16]. Compared with the photophysical processes, from capturing and converting powered photons to generate separated electrons/holes on surface active sites, chemical reactions on the surface catalytic centers are paid less attention [17]. For boosting surface reactions, co-catalysts (e.g., supported metals) are most commonly used [18], with decreasing activation

energy or lowering overpotential as the most general but rough reason for explaining the mechanisms of accelerating reactions, as well as promoting the diffusion of energetic carriers [19]. However, the investigation and utilization of detailed activation and catalytic effects on the surface is also essential, not only for the mechanism study on the atomic-level, but also for building a desired effective and selective artificial photocatalytic system, such as the highly efficient dark reaction stage in the natural photosynthesis processes [20].

Halide perovskites and their derivatives, with intrinsic and unique optoelectronic and physicochemical properties [21–24], such as wide absorption spectrum, large extinction coefficient, low exciton binding energy, fast charge carrier mobility, high defect tolerance, as well as unusual surface halide chemical states, have become emerging photocatalysts for various chemical conversions [25–28]. Lead-free halide perovskites possess cations with similar electron configurations of toxic Pb<sup>2+</sup> [29], showing great potentials as green and practical

\* Corresponding authors at: Key Laboratory of Eco-materials Advanced Technology, College of Materials Science and Engineering, Fuzhou University, Fuzhou 350108, China.

E-mail addresses: [huanghanlin@fzu.edu.cn](mailto:huanghanlin@fzu.edu.cn) (H. Huang), [chengkai\\_yang@fzu.edu.cn](mailto:chengkai_yang@fzu.edu.cn) (C. Yang), [yuyan@fzu.edu.cn](mailto:yuyan@fzu.edu.cn) (Y. Yu), [zgrou@nju.edu.cn](mailto:zgrou@nju.edu.cn) (Z. Zou).

<https://doi.org/10.1016/j.apcatb.2022.122146>

Received 30 September 2022; Received in revised form 3 November 2022; Accepted 6 November 2022

Available online 7 November 2022

0926-3373/© 2022 Elsevier B.V. All rights reserved.

photocatalysts [30–33]. Bismuth-based bromide perovskite derivatives (e.g.,  $\text{Cs}_3\text{Bi}_2\text{Br}_9$ ) [34] with all inorganic components exhibit relatively stable chemical properties while exposed to oxygen and light irradiation, and possess thermodynamically appropriate energy band structures related to p orbitals of Bi and Br [35]. Heterojunction construction (hybridized with other functional semiconductors) is usually employed as a useful strategy to boost the photocatalytic processes of these lead-free and promising candidates [34,36–39]. However, halide perovskites in heterojunction structures, have been simply and traditionally considered as semiconductors, only playing roles of harvesting photons, providing and accepting electrons/holes based on the theory of energy band [40]. The activation effect on the surface of halide perovskites, strongly related to the reaction rates of surface chemical reactions and the photocatalytic efficiency, is rarely concerned [41]. In contrast, the catalytic mechanisms of oxide-type perovskites, have already been studied and applied in some classical catalytic processes [42,43].

Aromatic  $\text{C}(\text{sp}^3)\text{-H}$  bond conversion [44,45], a thermodynamically challenging but important reaction for catalytic science and industry [46], is used as a model reaction in this study. To achieve an efficient activation for  $\text{C}(\text{sp}^3)\text{-H}$  bond, photocatalysis is a useful strategy under mild conditions. Thus, the delicate design of the photocatalytic system is required, with the integration of light-driving force for redox reactions and surface activation effects for the conversion of key intermediates.

Herein, a photoactivated lead-free halide perovskite-based hybrid with boosting photoelectrical effects and synergistic surface activation mechanisms, enables an efficient and selectively aromatic  $\text{C}(\text{sp}^3)\text{-H}$  conversion process, under air atmosphere and visible light (Scheme 1). A novel class of hybridized photocatalyst consisted of a lead-free halide perovskite derivative,  $\text{Cs}_3\text{Bi}_2\text{Br}_9/\text{CdS}$ , is developed for the first time and employed for the photocatalytic conversion of various aromatic hydrocarbons towards corresponding aldehydes or ketones as major products. A high activity is achieved with a conversion rate of ethylbenzene up to  $19.54 \text{ mmol g}^{-1} \text{ h}^{-1}$  and a maintained high selectivity (>85%) of benzaldehyde converted from toluene is obtained in a long-term

reaction, as well. More importantly, in addition to the enhancement of charge separation arising from the heterojunction structure and proper positions of energy bands, a new and efficient surface catalytic processes for the transformation of key intermediates, from benzyl radicals and superoxide anions to aldehydes, on the surface of  $\text{Cs}_3\text{Bi}_2\text{Br}_9$  perovskite derivative is observed and proved by density functional theory (DFT) simulations. The unique surface activation effects originate from the interaction between adsorbed species and surface sites (mainly  $\text{Cs}^+/\text{Br}^-$ ) of  $\text{Cs}_3\text{Bi}_2\text{Br}_9$ , leading to lower energy states and proper structures of reaction intermediates.

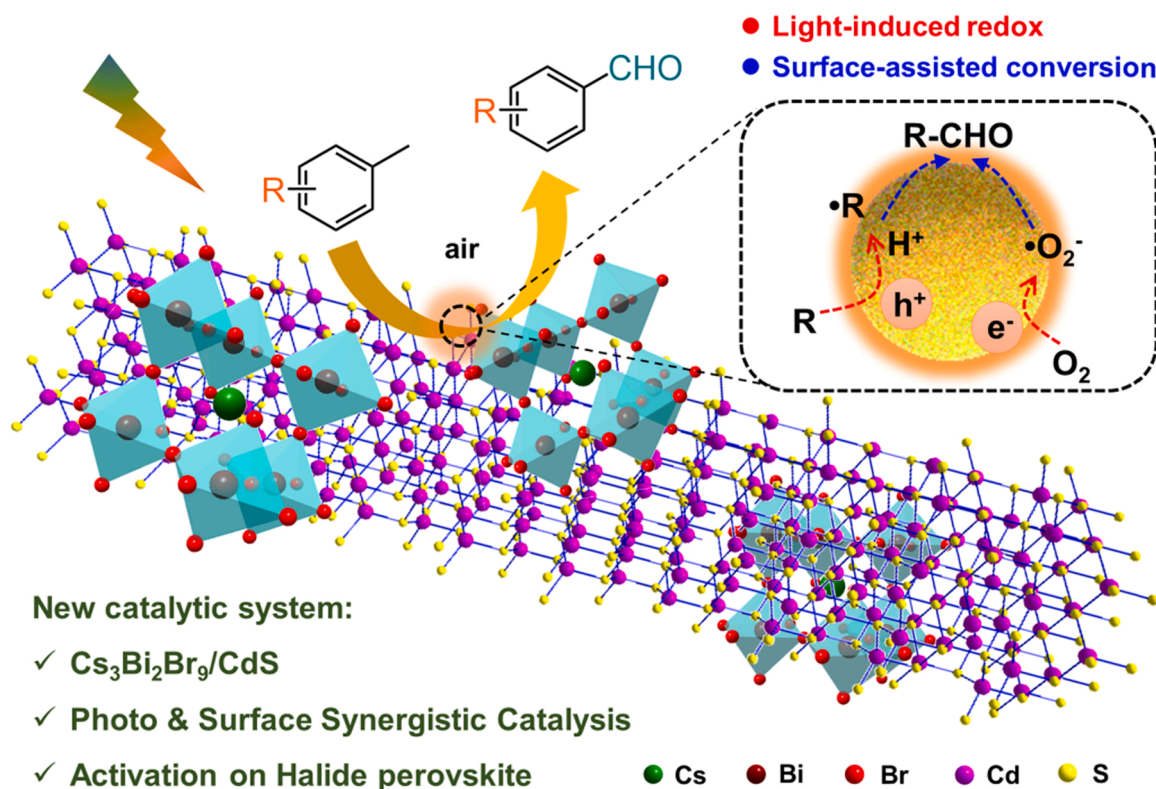
## 2. Experimental section

### 2.1. Materials

$\text{CsBr}$  (Aladdin),  $\text{BiBr}_3$  (Macklin), toluene (Sinopharm), benzaldehyde (Alfa Aesar), benzylalcohol (Sinopharm), ethanol (Sinopharm), acetonitrile (Sinopharm),  $\text{CdCl}_2 \cdot 2.5\text{H}_2\text{O}$  (Sinopharm),  $\text{CH}_4\text{N}_2\text{S}$  (Sinopharm), ethylenediamine (Sinopharm), 2,2,6,6-Tetramethylpiperidine 1-oxyl (TEMPO, Aladdin), 1,4-Benzoquinone (PBQ, Sinopharm), Ammonium oxalate (AO, Aladdin), Sodium azide (SA, Sinopharm), 5,5-dimethyl-1-pyrroline N-oxide (DMPO, Macklin), dimethyl sulfoxide (DMSO, Aladdin), butylated hydroxytoluene (BHT, Alfa Aesar), sodium oxalate (SO, Sinopharm), Tetrabutylammonium hexafluorophosphate (TBAPF6, Sinopharm), Ethylacetate (Aladdin),  $\text{Na}_2\text{SO}_4 \cdot 9\text{H}_2\text{O}$  (Aladdin). All of the reagents were commercially available and used without further purification.

### 2.2. Preparation of photocatalysts

Preparation of CdS nanorods. Synthesis of CdS nanorod: 4.62 g  $\text{CdCl}_2 \cdot 2.5\text{H}_2\text{O}$  and 4.62 g  $\text{CH}_4\text{N}_2\text{S}$  were completely dissolved in 60 mL ethylenediamine and the mixture was sealed into a Teflon-lined stainless steel autoclave. Hydrothermal treatment was conducted by increasing



**Scheme 1.** Schematic illustrations for the photocatalytic conversion of aromatic  $\text{C}(\text{sp}^3)\text{-H}$  bonds with  $\text{Cs}_3\text{Bi}_2\text{Br}_9/\text{CdS}$  hybrid photocatalyst under air and visible light, with the synergistic activation of photo and surface catalysis.

the temperature to 160 °C at 5 °C/min and kept at 160 °C for 60 h. Finally, the product was cooled to room temperature naturally, washed with ultrapure water and ethanol for 3 times, followed by drying under vacuum at 60 °C for 12 h.

Preparation of  $\text{Cs}_3\text{Bi}_2\text{Br}_9$  nanoparticles.  $\text{CsBr}$  (0.25 mmol) was dissolved into a mixed solvent (4 mL ethanol and 1 mL acetonitrile), the mixture was stirred at 50 °C for 2 h to form a solution. And then,  $\text{BiBr}_3$  (0.20 mmol) solution with a mixed solvent (4 mL ethanol and 1 mL acetonitrile) was slowly dropped into the above solution with the  $\text{CsBr}$  precursor, followed by stirring at 50 °C for 1 h. Finally, the product was washed with ethanol three times and centrifuged at 3000 rpm for 4 min. The yellow particles were obtained after dried under vacuum at 60 °C overnight.

Preparation of  $\text{Cs}_3\text{Bi}_2\text{Br}_9/\text{CdS}$ . The as-prepared  $\text{CdS}$  (100 mg) products were dispersed into 5 mL mixed solvent (4 mL ethanol and 1 mL acetonitrile) then added in a 25 mL round-bottom flask. Then the suspension mixture was stirred at 50 °C for 20 min.  $\text{CsBr}$  (0.25 mmol) and  $\text{BiBr}_3$  (0.2 mmol) were dissolved into a mixed solvent (4 mL ethanol and 1 mL acetonitrile), respectively, as precursors for the synthesis of  $\text{Cs}_3\text{Bi}_2\text{Br}_9$ . Then,  $\text{CsBr}$  solution was slowly dropped into the above mentioned suspension mixture of  $\text{CdS}$  within 5 min, followed by stirring with 550 rpm at 50 °C for 5 h. After that,  $\text{BiBr}_3$  solution was added into the above suspension within 5 min, and then stirred at 50 °C for 1 h, and then cooled to room temperature naturally. Finally, the crude product was washed with ethanol three times and centrifuged at 3000 rpm for 4 min, and then dried under vacuum at 60 °C overnight.

### 2.3. Photocatalytic performance test

For a typical photocatalytic experiment, 2 mg photocatalyst was dispersed in toluene (5 mL) and then added in a 25 mL schlenk glass tube. The liquid suspension was sealed in the tube under an air atmosphere (0.1 MPa). The reaction mixture was irradiated by the Xe lamp (PLS-SXE 300 C, Perfect light, China) with a 420 nm filter for a certain period of time. The products were analyzed quantitatively by a gas chromatography (GC-8A, Shimadzu, Japan) with a SH-Rtx-1 column utilizing an external standard method, and qualitatively by a gas chromatography-mass spectrometry (GC-MS, QP2020 NX, Shimadzu, Japan) with a SH-Rxi-5Sil column. A series of monochromatic lights with different wavelengths (405, 473, 532 and 637 nm) were also used for photocatalytic performance test. Tert-butyl alcohol (TBA), sodium azide (SA), Benzoic acid (BA), 1,4-benzoquinone (PBQ), sodium oxalate (SO), 2,2,6,6-Tetramethyl-1-piperidinyloxy (TEMPO) and butylhydroxytoluene (BHT) were used as scavengers for capturing active species during the photoreaction.

### 2.4. Characterizations

Scanning electron microscope (SEM, SUPRA 55, Carl Zeiss, Germany) characterization was obtained using an acceleration voltage of 10 V. Transmission electron microscopy (TEM) and high-resolution transmission electron microscopy (HRTEM, Talos F200i FEI, FEI, America) were conducted with an accelerating voltage of 300 kV. X-ray diffraction (XRD, Miniflex600, Journalism Company, Japan) was performed with a  $\text{Cu K}\alpha$  radiation, using a tube voltage of 40 kV and a current of 30 mA. X-ray photoelectron spectroscopy (XPS, Thermo Fisher Scientific, K-Alpha<sup>+</sup>, USA) measurement was conducted with a monochromatic Al anode. Light absorption curves were recorded by UV-vis diffuse reflectance spectra (UV-vis DRS, Cary 500, Varian). Radicals during the reaction were detected by electron spin resonance spectrometer (ESR, EMXnano, German bruck, German). Inductively coupled plasma-atomic emission spectrometry (ICP-AES) was used for the analysis of the components in the photocatalyst. The transient photocurrent response spectroscopy (TPRS) and electrochemical impedance spectroscopy (EIS) were obtained on the electrochemical workstation (TPRS: CHI 660E, Shanghai Chenhua Instrument Co., LTD,

China; EIS: Parstat MC Princeton, USA) in a three-electrode system (reference electrode:  $\text{Ag}/\text{AgCl}$  with saturated  $\text{KCl}$ ; counter electrode:  $\text{Pt}$ ), the working electrode was fabricated by dropping the suspension liquid (5 mg powders dispersed in 1 mL toluene) on the FTO glass with a 0.25  $\text{cm}^2$  working area. The electrolyte was tetrabutylammonium hexafluorophosphate dissolved in ethyl acetate (0.1 M). Mott-Schottky measurements were carried out using an electrochemical working station (CHI 660E, Shanghai Chenhua Instrument Co., LTD, China) with the applying voltage range:  $-1.2 \text{ V} \sim +1.2 \text{ V}$ , and the electrolyte was used a  $\text{Na}_2\text{SO}_4$  aqueous solution (0.2 M). In situ XPS measurement of samples was conducted under a visible light illumination ( $\lambda > 420 \text{ nm}$ ,  $\sim 100 \text{ mW}/\text{cm}^2$ ) through a window on the instrument (Thermo VG, ESCALAB 250, USA).

### 2.5. Calculation and modeling

All calculations reported in this work were performed using the Vienna Ab initio simulation program (VASP) [47]. The interaction between the ionic core and valence electrons was described by the projector augmented wave method (PAW). The total energy convergence and the forces on each atom were set to be lower than  $10^{-6} \text{ eV}$  and  $0.02 \text{ eV } \text{\AA}^{-1}$ . Energy cutoff of 520 eV for the plane wave basis set was used for the structure optimization analysis. A  $1 \times 1 \times 1$  k-point mesh was used for the Brillouin zone sampling. The Perdew-Burke-Ernzerhof functional with generalized gradient approximation was employed to describe the electron exchange and correlation energy [48]. Surface Models. For the (100) surface of  $\text{Cs}_3\text{Bi}_2\text{Br}_9$ , we use a  $2 \times 2$  slab including one atomic layer. For the (100) surface of hexagonal wurtzite  $\text{CdS}$ , we use a  $2 \times 2$  slab including two atomic layers with 8 Cd atoms and 8 S atoms in each slab. A vacuum with the thickness of about 15 Å is included to avoid interactions between the repeating slabs, and all of the atoms were allowed to be fully relaxed. Adsorption catalysis. Adsorption catalysis. All reactions occur on the slab to account for the charge accuracy of the chemical reaction process and the system is in a stable adsorption state at all times.

## 3. Results and discussion

### 3.1. Photocatalytic performance of $\text{C}(\text{sp}^3)\text{-H}$ conversion

Toluene molecule was initially used as the model substrate to evaluate the photocatalytic performance for  $\text{C}(\text{sp}^3)\text{-H}$  conversion, in air atmosphere and under visible light ( $\lambda > 420 \text{ nm}$ ). The characterizations of products, benzaldehyde and benzyl alcohol, are displayed in Fig. S2 with their corresponding spectrums of gas chromatography (Fig. S2a) and mass spectrometry (Fig. S2b and c). As shown in Fig. 1a, poor activities were observed for pristine  $\text{CdS}$  ( $0.18 \text{ mmol g}^{-1} \text{ h}^{-1}$ ) and  $\text{Cs}_3\text{Bi}_2\text{Br}_9$  ( $0.97 \text{ mmol g}^{-1} \text{ h}^{-1}$ ). To our delight, conversion rates enhanced significantly while utilizing  $\text{Cs}_3\text{Bi}_2\text{Br}_9/\text{CdS}$  hybrid as the photocatalyst. An optimized activity reached up to  $6.79 \text{ mmol g}^{-1} \text{ h}^{-1}$ , with benzaldehyde as the main product, showing a 37.6-fold and 7.1-fold enhancement compared with that of pristine  $\text{CdS}$  and  $\text{Cs}_3\text{Bi}_2\text{Br}_9$ , which reaches the state-of-the-art levels in the photocatalytic oxidation used halide perovskites or their derivatives (Table S1) [49–56]. The photocatalytic performance of  $\text{Cs}_3\text{Bi}_2\text{Br}_9$  (x)/ $\text{CdS}$  hybrid (x values are defined as 1, 2, 4, representing different adding amounts the synthesis of  $\text{Cs}_3\text{Bi}_2\text{Br}_9$ , see the Experimental Section for details) catalysts initially improved and then dropped a little with the increasing amount of  $\text{Cs}_3\text{Bi}_2\text{Br}_9$  (the hybrid of  $\text{Cs}_3\text{Bi}_2\text{Br}_9$  (2)/ $\text{CdS}$  has the optimal performance), which may be ascribed to an over injection of electrons, less accessible active sites and a more serious recombination of photoinduced carriers due to larger particles or excess exposed sites of  $\text{Cs}_3\text{Bi}_2\text{Br}_9$ . The molar ratio between  $\text{Cs}_3\text{Bi}_2\text{Br}_9$  and  $\text{CdS}$  are 0.072:1 ( $x = 0.1$ ), 0.144:1 ( $x = 0.2$ ) and 0.288:1 ( $x = 0.4$ ), respectively, according to the characterization results from ICP-AES. In order to demonstrate the potential practical application of this system, a



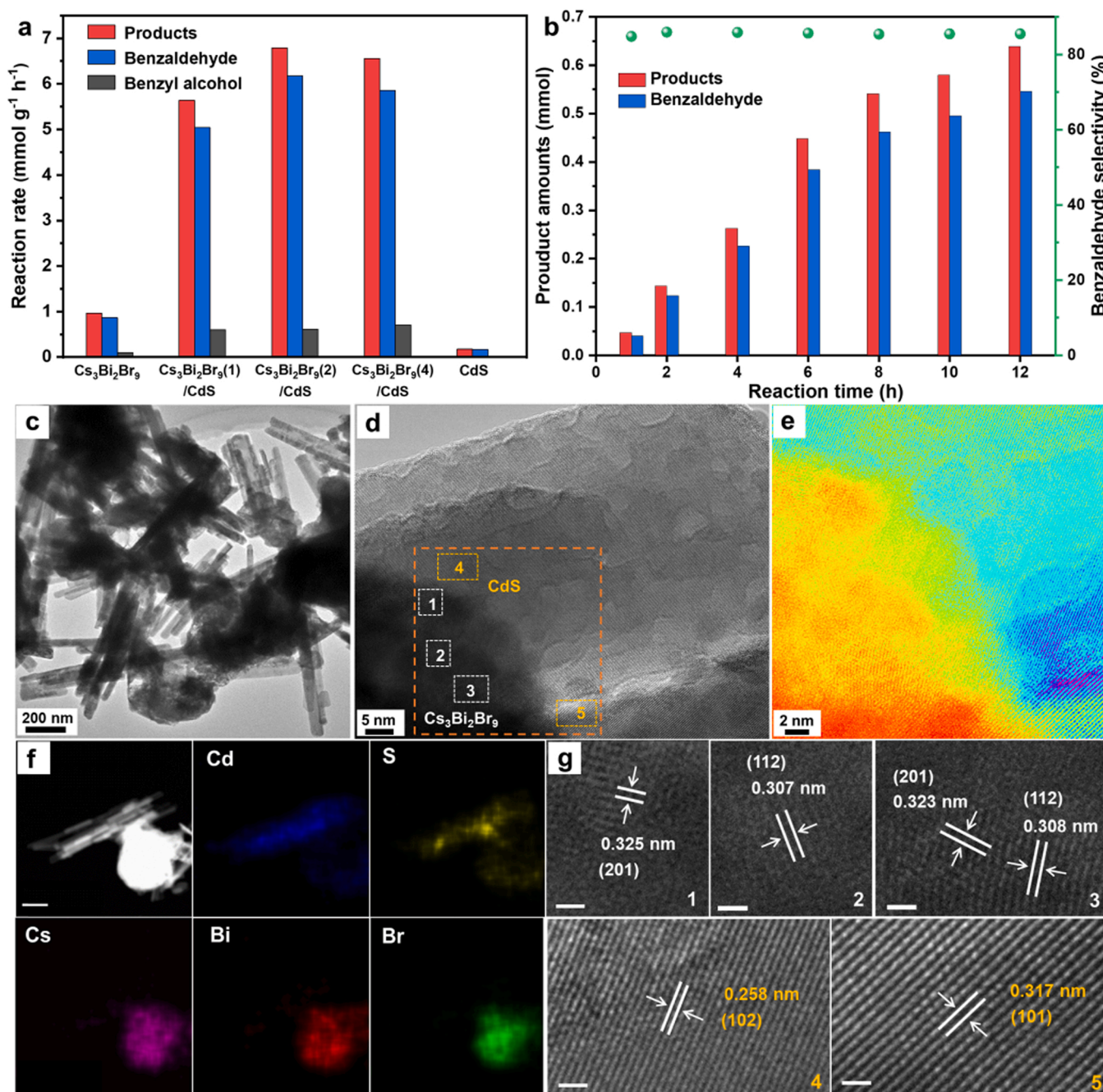


**Fig. 1.** (a) Photocatalytic activities (conversion rate of toluene, production rate of benzaldehyde and benzyl alcohol) of toluene oxidation utilizing Cs<sub>3</sub>Bi<sub>2</sub>Br<sub>9</sub>/CdS, Cs<sub>3</sub>Bi<sub>2</sub>Br<sub>9</sub> and CdS as photocatalysts. Reaction conditions: 0.1 MPa air, room temperature (293 K), 5 mL toluene, 2 mg photocatalyst, 2 h irradiation ( $\lambda > 420$  nm). (b) Long-term activity of total production rate and benzaldehyde production rate, and the time-dependence of selectivity of benzaldehyde. TEM (c) and HRTEM (d) image of Cs<sub>3</sub>Bi<sub>2</sub>Br<sub>9</sub>/CdS hybrid. (e) Color snapshot of the square in (d) showing the clearer interface between Cs<sub>3</sub>Bi<sub>2</sub>Br<sub>9</sub> and CdS. (f) HAADF-STEM image of a typical area of Cs<sub>3</sub>Bi<sub>2</sub>Br<sub>9</sub>/CdS hybrid and corresponding elemental mappings of Cd, S, Cs, Bi, Br. (g) Lattice fringes of Cs<sub>3</sub>Bi<sub>2</sub>Br<sub>9</sub> and CdS surfaces.

long-term photocatalytic experiment was also performed. The amounts of products increased almost linearly with prolonging the reaction time under irradiation. Although the reaction rate showed a decline while increasing the irradiation time, which may be caused by the generated water after the oxidation of toluene by oxygen in air, leading to the slow deactivation of the moisture sensitive halide perovskites [57,58], anhydrous agents can be used to remove produced water and regenerate the activity. To our delight, the selectivity of the value-added product, benzaldehyde, maintained above 85% without obvious change during the whole reaction process (Fig. 1b), which shows the stability and robustness of our photocatalytic system.

The universality of Cs<sub>3</sub>Bi<sub>2</sub>Br<sub>9</sub>/CdS for photocatalytic transformation of other aromatic hydrocarbons was also investigated. As shown in Fig. S1, various types of reaction substrates, such as paraxylene, ethylbenzene, bromotoluene and chlorotoluene, can be efficiently converted under the similar mild conditions (air, room temperature, visible light). Spectrums of gas chromatography and mass spectrometry of various products, with corresponding aldehydes (ketones) and alcohols are shown in Figs. S2-S9. Toluene derivatives with an electron-donating group, such as -CH<sub>3</sub>, have higher conversion rates (7.17 and 19.54 mmol g<sup>-1</sup> h<sup>-1</sup>) than that of toluene [59]. Besides, p-bromotoluene showed an excellent reaction activity (17.96 mmol g<sup>-1</sup> h<sup>-1</sup>) due to its

coexisting electron donating effect derived from the p- $\pi$  conjugation except the weak electron withdrawing effect. In comparison, p-bromotoluene also exhibited a higher activity than that of its isomers, o-bromotoluene ( $7.03 \text{ mmol g}^{-1} \text{ h}^{-1}$ ) and m-bromotoluene ( $0.65 \text{ mmol g}^{-1} \text{ h}^{-1}$ ), which is mainly ascribed from the steric hindrance, leading to an impact on the adsorption and activation of reactants and intermediates during the reaction. However, p-chlorotoluene showed a poorer activity ( $4.34 \text{ mmol g}^{-1} \text{ h}^{-1}$ ) than that of p-bromotoluene, because of its stronger electron-withdrawing ability. A high activity ( $13.99 \text{ mmol g}^{-1} \text{ h}^{-1}$ ) for p-nitrotoluene is also obtained, although with an electron-withdrawing group,  $-\text{NO}_2$ , which may be ascribed to the higher reaction temperature of 373 K required for melting of this solid substrate. More importantly, the majority of aromatic hydrocarbons were selectively converted into their corresponding aldehydes or ketones as main products, which are high value-added compounds for chemical and pharmaceutical industry. These results demonstrate the universal application of  $\text{Cs}_3\text{Bi}_2\text{Br}_9/\text{CdS}$  hybrid photocatalyst for the functionalization of  $\text{C}(\text{sp}^3)\text{-H}$  bonds in various aromatic hydrocarbons. Controlled experiments (Fig. S10) demonstrate that both light irradiation and catalyst are necessary.

### 3.2. Structure characterizations and photoelectrical properties

The synthetic process of  $\text{Cs}_3\text{Bi}_2\text{Br}_9/\text{CdS}$  hybrid was based on an in-situ growth approach (Fig. S11) [28], with the formation of  $\text{Cs}_3\text{Bi}_2\text{Br}_9$  nanoparticles (reaction between precursors, cesium bromide and bismuth bromide in a mixed ethanol/acetonitrile solvent) on the surface of as-prepared CdS nanorods. Scanning electron microscopy (SEM) images of pure CdS nanorods and  $\text{Cs}_3\text{Bi}_2\text{Br}_9$  nanoparticles are shown in Fig. S12. The transmission electron microscopy (TEM) image (Fig. 1c) displays the morphology of  $\text{Cs}_3\text{Bi}_2\text{Br}_9/\text{CdS}$  hybrid, with  $\text{Cs}_3\text{Bi}_2\text{Br}_9$  particles in close proximity to clusters of CdS nanorods. The high-angle annular dark-field scanning TEM (HAADF-STEM) image coupled with the energy dispersive X-ray spectroscopy (EDX) were used to investigate the

compositional distribution of  $\text{Cs}_3\text{Bi}_2\text{Br}_9/\text{CdS}$  hybrid. As shown in Fig. 1f, Cd, S, Cs, Bi and Br elements are homogeneously distributed in the corresponding area of hybrid, respectively. High-resolution TEM (HRTEM) images (Fig. 1d, e and g) exhibit the interface and lattice fringes. The interface between  $\text{Cs}_3\text{Bi}_2\text{Br}_9$  and CdS is shown in Fig. 1d. An enlarged boundary structure with clearer lattice fringes is presented as Fig. 1e with color snapshot. Distances of crystal faces are identified in Fig. 1g, in which 0.323 or 0.325 nm, 0.307 or 0.308 nm, corresponding to (201) and (112) planes of  $\text{Cs}_3\text{Bi}_2\text{Br}_9$ , while 0.258 and 0.317 nm corresponding to (102) and (101) planes of CdS, respectively. X-ray diffraction (XRD) patterns of pristine  $\text{Cs}_3\text{Bi}_2\text{Br}_9$  and CdS are shown in Fig. S13 and both  $\text{Cs}_3\text{Bi}_2\text{Br}_9$  and CdS exhibit the hexagonal crystal structure, corresponding to PDF#44-0714 and PDF#41-1079, respectively. XRD patterns of  $\text{Cs}_3\text{Bi}_2\text{Br}_9/\text{CdS}$  with different amounts of  $\text{Cs}_3\text{Bi}_2\text{Br}_9$  are also displayed in Fig. S13 and the height of peaks of  $\text{Cs}_3\text{Bi}_2\text{Br}_9$  become stronger with its loading amounts increasing. Photocatalysts after reaction were characterized by XRD (Fig. S14) and SEM (Fig. S15), without obvious change of their crystal structure and hybrid morphology, which demonstrates a satisfied stability of  $\text{Cs}_3\text{Bi}_2\text{Br}_9/\text{CdS}$  under light illumination, as well. All results above reveal the successful synthesis of  $\text{Cs}_3\text{Bi}_2\text{Br}_9/\text{CdS}$  hybrid. Besides, only 0.25% of  $\text{Cd}^{2+}$  of CdS dissolved into the solvent according to the testing results from ICP-AES, which demonstrates the stability of CdS in this photo reaction system with negligible photocorrosion.

### 3.3. Photocatalytic activation

The relationship between reaction rates and wavelengths of incident lights was investigated. Activities correspond well with the optical absorption spectrum of CdS (Fig. 2a), which reveals that the light harvesting of CdS semiconductor plays a key role. It is believed that  $\text{Cs}_3\text{Bi}_2\text{Br}_9$  in the hybrid also participates in the photocatalytic conversion, proved by its intrinsic photocatalytic activity and promoting effect in  $\text{Cs}_3\text{Bi}_2\text{Br}_9/\text{CdS}$ . Transient photocurrent response spectroscopy (TPRS)

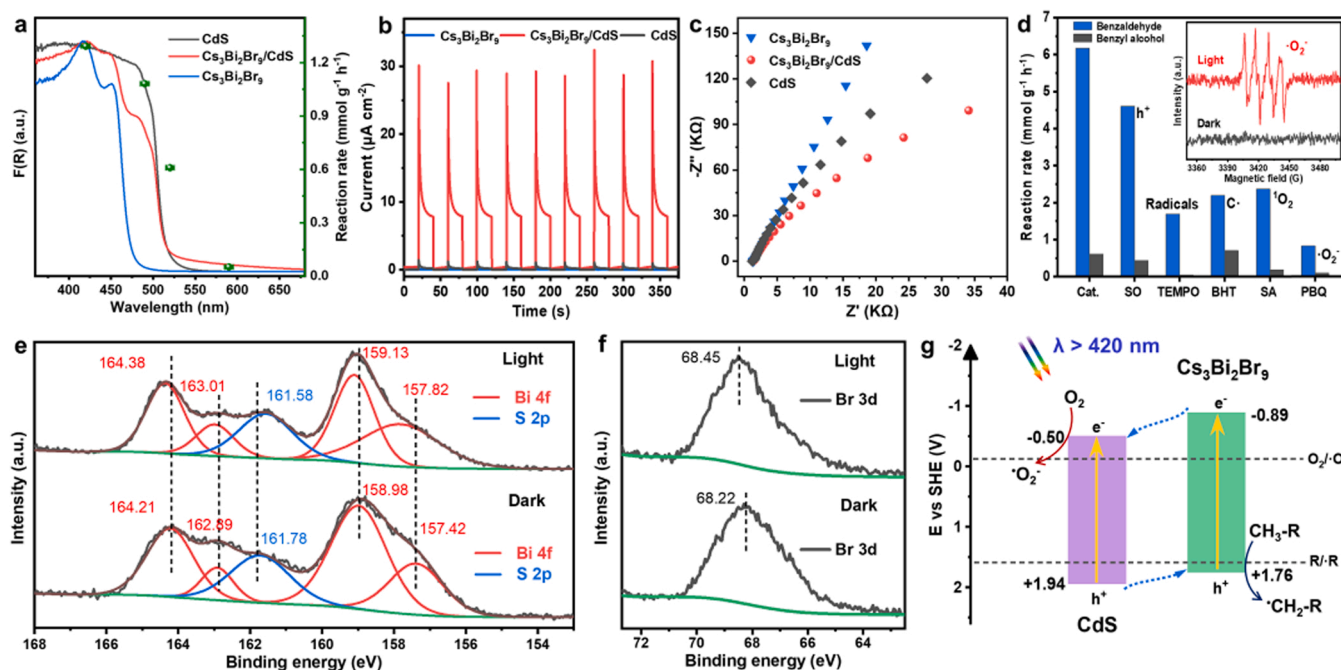


**Fig. 2.** (a) Photocatalytic conversion rate of toluene under monochromatic incident lights with different wavelengths and the optical absorption spectra of  $\text{Cs}_3\text{Bi}_2\text{Br}_9/\text{CdS}$ ,  $\text{Cs}_3\text{Bi}_2\text{Br}_9$  and CdS. TPRS (b) and EIS (c) curves of  $\text{Cs}_3\text{Bi}_2\text{Br}_9/\text{CdS}$ ,  $\text{Cs}_3\text{Bi}_2\text{Br}_9$  and CdS. (d) Photocatalytic conversion rates of toluene without additives or in the presence of different scavengers for trapping various intermediates during the photoreaction. Inset is the ESR patterns in the dark condition or under visible light irradiation with DMPO as the trapping agent in the mixed liquid system with photocatalysts and toluene, 0.1 MPa air. *In-situ* XPS spectra of Bi 4f, S 2p (e) and Br 3d (f) of  $\text{Cs}_3\text{Bi}_2\text{Br}_9/\text{CdS}$  in the dark or light irradiation condition. (g) Energy band structures of  $\text{Cs}_3\text{Bi}_2\text{Br}_9$  and CdS, and the proposed transfer pathways for photoinduced carriers and redox reactions under visible light ( $\lambda > 420 \text{ nm}$ ).

combined with electrochemical impedance spectroscopy (EIS) were further utilized to investigate the separation and transfer of carriers in the hybrid photocatalyst. As shown in Fig. 2b,  $\text{Cs}_3\text{Bi}_2\text{Br}_9/\text{CdS}$  hybrid exhibits a significantly enhanced photocurrent response compared with those of  $\text{Cs}_3\text{Bi}_2\text{Br}_9$  and CdS, indicating a much higher rate of separation and transfer for photoinduced electrons/holes. Besides, as illustrated in Fig. 2c,  $\text{Cs}_3\text{Bi}_2\text{Br}_9/\text{CdS}$  hybrid displays a decreased resistance for the transportation of carriers based on semicircles of Nyquist plots of different photocatalysts obtained from the measurement of electrochemical impedance. Difference of photoelectrochemical properties between the hybrid photocatalyst ( $\text{Cs}_3\text{Bi}_2\text{Br}_9/\text{CdS}$ ) and pristine ones ( $\text{Cs}_3\text{Bi}_2\text{Br}_9$  and CdS) reveals that the efficiency for extracting and utilizing photogenerated carriers has been improved after the formation of heterojunction.

To further clarify the photocatalytic reaction processes, various trapping agents were used to capture various intermediates under visible light illumination, in air atmosphere (Fig. 2d). Generally, for the attack and cleavage of  $\text{C}(\text{sp}^3)\text{-H}$  bonds, photo-generated holes ( $\text{h}^+$ ) are the major oxidizing agents [60], which can be captured by sodium oxalate (SO). In our experiment, photocatalytic activity declined after the addition of SO, indicating  $\text{h}^+$  is a key intermediate. Besides, radicals are usually active species in photocatalytic organic transformations. Therefore, a scavenger of 2,2',6,6'-tetramethylpiperidine-1-oxyl (TEMPO) was added to capture different types of radicals and the reaction rate significantly decreased, which demonstrates that the photocatalytic conversion of  $\text{C}(\text{sp}^3)\text{-H}$  bond is a radical-mediated reaction [61]. Next, butylated hydroxytoluene (BHT), a scavenger capturing carbon-centered radicals, was added and a lowered rate was obtained, which demonstrates that benzyl radicals after the cleavage of  $\text{C}(\text{sp}^3)\text{-H}$  bonds are also important. Moreover, active oxygen species, such as singlet oxygen ( $^1\text{O}_2$ ) and superoxide anions ( $\cdot\text{O}_2^-$ ), are vital intermediates in this photoreaction, with an obvious drop of activity after the introduction of sodium azide (SA) for  $^1\text{O}_2$ , and 1,4 benzoquinones (PBQ) for  $\cdot\text{O}_2^-$ . *In-situ* electron spin resonance (ESR) results (inset of Fig. 2d) show that  $\cdot\text{O}_2^-$  generated after visible light irradiation on  $\text{Cs}_3\text{Bi}_2\text{Br}_9/\text{CdS}$ ,  $\text{Cs}_3\text{Bi}_2\text{Br}_9$  (Fig. S16a) or CdS (Fig. S16b), captured by 5,5-dimethyl-1-pyrroline-N-oxide (DMPO), further indicating that  $\cdot\text{O}_2^-$  is one of the major intermediates.

In order to further investigate the transfer schemes of photo-induced carriers in the  $\text{Cs}_3\text{Bi}_2\text{Br}_9/\text{CdS}$  hybrid, *in-situ* X-ray photoelectron spectroscopy (XPS) under light illumination was performed, which has also been utilized to confirm the electron transfer pathway in reported literatures [62–64]. Transfer pathways of interfacial carriers between  $\text{Cs}_3\text{Bi}_2\text{Br}_9$  and CdS was studied. As shown in Fig. 2e, in the dark condition, peaks of binding energy of Bi 4f on the surface of  $\text{Cs}_3\text{Bi}_2\text{Br}_9/\text{CdS}$  can be resolved into four peaks (164.21 eV, 162.89 eV, 158.98 eV, 157.42 eV) [50,65] and 161.78 eV can be identified as the binding energy of S 2p [66]. After light irradiation, positive shifts of Bi 4f were observed (164.38 eV, 163.01 eV, 159.13 eV, 157.82 eV), which reveals that the electron density around Bi atoms decreased. Meanwhile, the binding energy of S 2p exhibited a negative shift (161.58 eV), which reveals that the electron density around S atoms increased. Therefore, electrons transferred from  $\text{Cs}_3\text{Bi}_2\text{Br}_9$  towards CdS under light irradiation. Moreover, the binding energy of Br 3d experienced a positive shift from 68.22 eV to 68.45 eV (Fig. 2f), which also demonstrates that  $\text{Cs}_3\text{Bi}_2\text{Br}_9$  become more electron deficient with electrons migrating to the surface of CdS. Besides, the binding energy of Cs 3d and Cd 3d showed a not obvious change after illumination (Fig. S17), which may be ascribed to the interaction between the  $\text{S}^{2-}$  and  $[\text{BiBr}_6]^{3-}$  in the interface of CdS and  $\text{Cs}_3\text{Bi}_2\text{Br}_9$  [67], instead of the  $\text{Cs}^+$  and  $\text{Cd}^{2+}$  sites. In addition, photodeposition of Rh metal was carried out with  $\text{Cs}_3\text{Bi}_2\text{Br}_9/\text{CdS}$  hybrid, illuminated with visible light, which is also one of the classic approaches to investigate the charge transfer pathway. As shown in Fig. S18, the majority of Rh metal particles are distributed on the CdS surface, which demonstrates that most of photo-generated electrons are accumulated on the CdS sites in electron-rich states.

Therefore, this result further suggests that excited electrons in  $\text{Cs}_3\text{Bi}_2\text{Br}_9$  mainly transfer to CdS.

Band structure, one of the most important properties of semiconductors, was also investigated.  $\text{Cs}_3\text{Bi}_2\text{Br}_9$  and CdS has a band gap energy of 2.65 eV and 2.44 eV, respectively, according to the Tauc plots (Fig. S19). The flat band potential of CdS is determined as  $-0.65$  V (vs Ag/AgCl) by Mott-Schottky method (Fig. S20), corresponding to  $-0.45$  V (vs SHE). Since the flat band potential of n-type semiconductor (e.g., CdS) is generally 0.05 V lower than the conduction band (CB) [68], thus,  $-0.50$  V is regarded as the position of conduction band of CdS in this study. Therefore, the position of valence band (VB) of CdS is calculated to be  $+1.94$  V (vs SHE). Besides, the position of valence band of  $\text{Cs}_3\text{Bi}_2\text{Br}_9$  is determined as  $+1.76$  V (vs SHE) by its XPS-valence band result (Fig. S21). As a result, the position of conduction of  $\text{Cs}_3\text{Bi}_2\text{Br}_9$  is  $-0.89$  V (vs SHE).

Photocatalytic processes under visible light on  $\text{Cs}_3\text{Bi}_2\text{Br}_9/\text{CdS}$  heterojunction is proposed (Fig. 2g) based on above results. Under visible light irradiation ( $\lambda > 420$  nm), energetic carriers including electrons ( $\text{e}^-$ ) and holes ( $\text{h}^+$ ) can be generated inside both  $\text{Cs}_3\text{Bi}_2\text{Br}_9$  and CdS, and distributed on each CB and VB, respectively, followed by the separation and migration to the surface. After that, electrons transfer from the CB of  $\text{Cs}_3\text{Bi}_2\text{Br}_9$  to that of CdS, meanwhile, holes migrate from the VB of CdS to that of  $\text{Cs}_3\text{Bi}_2\text{Br}_9$ .  $\text{O}_2$  can be reduced by  $\text{e}^-$  on the CB of CdS, generating  $\cdot\text{O}_2^-$  and aromatic alkanes ( $\text{CH}_3\cdot\text{R}$ ) can be oxidized by  $\text{h}^+$  on the VB of  $\text{Cs}_3\text{Bi}_2\text{Br}_9$ , to form benzyl radicals ( $\cdot\text{CH}_2\cdot\text{R}$ ). Finally, benzyl radicals react with  $\cdot\text{O}_2^-$  and mainly produce aldehydes after surface reaction steps [69].

### 3.4. Investigation of other roles for perovskite

It should be noted that  $\text{Cs}_3\text{Bi}_2\text{Br}_9$  has a larger bandgap (2.65 eV) than that of CdS (2.44 eV), leading to a narrower range of light absorption spectrum (Fig. 2a). In other words,  $\text{Cs}_3\text{Bi}_2\text{Br}_9$  could not absorb light with wavelength longer than 470 nm and electrons inside  $\text{Cs}_3\text{Bi}_2\text{Br}_9$  could not be excited over this wavelength. Therefore, while under light irradiation ( $\lambda > 470$  nm), electrons inside CdS can be excited to its CB, and the holes on the VB of CdS will transfer to that of  $\text{Cs}_3\text{Bi}_2\text{Br}_9$ . The difference of light absorption remind us to consider the other roles of  $\text{Cs}_3\text{Bi}_2\text{Br}_9$  without light excitation while CdS could be excited by light. In this case, the enhancement of photocatalytic activity is traditionally considered as the enhanced separation of carriers [70], and the semiconductor in the heterojunction without light absorption is regarded as a component only accepting carriers. However, except for the roles as electron acceptor or donor, the surface catalytic effects for the activation and conversion of key intermediates are always ignored, especially for the halide perovskites [71]. What is the role for  $\text{Cs}_3\text{Bi}_2\text{Br}_9$  in the  $\text{Cs}_3\text{Bi}_2\text{Br}_9/\text{CdS}$  hybrid in this study while under illumination with incident photons having smaller energy ( $\lambda > 470$  nm) than the bandgap of  $\text{Cs}_3\text{Bi}_2\text{Br}_9$ ? The surface catalytic effects, such as a co-catalyst, may also exist?

As is well known, the overall photocatalytic performance is determined by three key steps including the intensity of light absorption, the efficiency of charge separation, and the reaction rate on the surface. Therefore, we study the role for  $\text{Cs}_3\text{Bi}_2\text{Br}_9$  in the  $\text{Cs}_3\text{Bi}_2\text{Br}_9/\text{CdS}$  hybrid from the perspectives of above mentioned three key steps. The traditional photoelectrical effects were initially considered and studied. As shown in Fig. 3a, photocatalytic activity of  $\text{Cs}_3\text{Bi}_2\text{Br}_9/\text{CdS}$  under monochromatic incident light of 520 nm shows a significant enhancement (14.9-fold) compared with that of pristine CdS. However, the light absorption intensity of CdS is very close to that of  $\text{Cs}_3\text{Bi}_2\text{Br}_9/\text{CdS}$  at the same wavelength (520 nm, blue circle in Fig. 3a), which reveals that light absorption is not the key factor. Next, the effect of charge separation is also explored. As shown in Fig. 3b,  $\text{Cs}_3\text{Bi}_2\text{Br}_9/\text{CdS}$  exhibits a 25.3-fold enhancement (on the left of Fig. 3b) compared with that of CdS in terms of transient photocurrent response under irradiation across the whole visible light spectrum ( $\lambda > 420$  nm). It is noted that the enhancement is similar to that of photocatalytic activity (Fig. 1a). In a



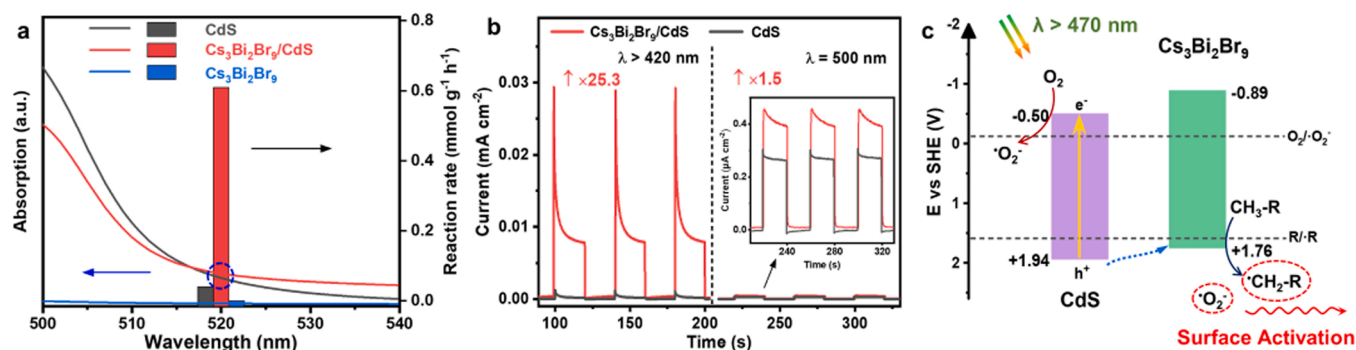


**Fig. 3.** (a) Optical absorption spectra of Cs<sub>3</sub>Bi<sub>2</sub>Br<sub>9</sub>/CdS, Cs<sub>3</sub>Bi<sub>2</sub>Br<sub>9</sub> and CdS beyond 500 nm and their corresponding photocatalytic performance at 520 nm. (b) TPRS curves of Cs<sub>3</sub>Bi<sub>2</sub>Br<sub>9</sub>/CdS and CdS under different light illumination conditions (λ > 420 nm or λ = 500 nm). Inset is an enlarged picture of TPRS curves of Cs<sub>3</sub>Bi<sub>2</sub>Br<sub>9</sub>/CdS and CdS with light illumination at 500 nm. (c) Plausible surface activation on Cs<sub>3</sub>Bi<sub>2</sub>Br<sub>9</sub> during photocatalysis under illumination beyond 470 nm.

contrast, for the aspect of enhancement of photocurrent response (representing the separation effect of photo-induced carriers), Cs<sub>3</sub>Bi<sub>2</sub>Br<sub>9</sub>/CdS only exhibits a 1.5-fold enhancement (on the right of Fig. 3b) under an illumination with a wavelength of 500 nm, which is much smaller than the increase amplitude of photocatalytic activity (14.9-fold, Fig. 3a). Besides, both Cs<sub>3</sub>Bi<sub>2</sub>Br<sub>9</sub>/CdS and CdS showed much weaker photocurrent response. These results reveal the charge separation is not the major role of Cs<sub>3</sub>Bi<sub>2</sub>Br<sub>9</sub>, as well. Therefore, it is believed that the surface activation for the conversion of intermediate radicals on Cs<sub>3</sub>Bi<sub>2</sub>Br<sub>9</sub> are reasonable (Fig. 3c).

### 3.5. Surface activation

Reaction pathways for photocatalytic conversion of alkanes with oxygen [49], utilizing Cs<sub>3</sub>Bi<sub>2</sub>Br<sub>9</sub> or CdS as the catalyst, are shown in Fig. S22 (Ph-CH<sub>3</sub> referred to toluene, was used as the model substrate). Firstly, e<sup>-</sup> and h<sup>+</sup> are generated after light excitation and accumulated on the surface sites. Next, O<sub>2</sub> are reduced by e<sup>-</sup> to form ·O<sub>2</sub> and toluene are oxidized by h<sup>+</sup> to form benzyl radicals (Ph-CH<sub>2</sub>·). Then, ·O<sub>2</sub> can react with benzyl radicals to produce 1-(hydroperoxymethyl) benzene (Ph-CH<sub>2</sub>OOH) via a peroxide anion (Ph-CH<sub>2</sub>OO<sup>-</sup>) intermediate [72]. Finally, benzaldehyde (PhCHO) is produced after the elimination of water from Ph-CH<sub>2</sub>OOH [68].

Based on these basic reaction processes, density functional theory

(DFT) calculations were conducted to explore the energy change during the reaction on the Cs<sub>3</sub>Bi<sub>2</sub>Br<sub>9</sub> (100) and CdS (100) surface from the perspective of thermodynamics. As shown in Fig. 4a, the surface of Cs<sub>3</sub>Bi<sub>2</sub>Br<sub>9</sub> (100) is more thermodynamically favourable for the conversion of key intermediates, which might be ascribed to the more effective catalytic effects on the Cs<sub>3</sub>Bi<sub>2</sub>Br<sub>9</sub> surface, facilitating the formation of transition states. Moreover, calculation results for the change of Gibbs energy (ΔG) are also summarized in Fig. S23 and Table S2. Usually, lower values of ΔG represent easier reaction processes. From the perspective of the whole process for the conversion of key intermediates, it is believed that more effective catalytic effects occur on Cs<sub>3</sub>Bi<sub>2</sub>Br<sub>9</sub> surface.

The structure evolutions of adsorbed intermediates during the conversion on the surface were also investigated by the DFT method, which further explain the activation and catalytic effects from the perspective of the cleavage and formation of bonds. Reaction processes on the Cs<sub>3</sub>Bi<sub>2</sub>Br<sub>9</sub> (100) surface is shown in Fig. 4b, showing the interaction between intermediates and substrate. The benzyl radical and H<sup>+</sup> adsorbed on the surface of Cs<sub>3</sub>Bi<sub>2</sub>Br<sub>9</sub> (100), via C-Cs (3.80 Å) and H-Br (1.52 Å) bond, respectively. The following reaction between ·O<sub>2</sub> and the benzyl radical, defined as O<sub>2</sub> insertion, produces peroxide anion (PhCH<sub>2</sub>OO<sup>-</sup>) intermediate, interacting with Cs<sub>3</sub>Bi<sub>2</sub>Br<sub>9</sub> (100) via a single O-Cs bond (2.78 Å). Next, a proton transfer reaction proceeds between PhCH<sub>2</sub>OO<sup>-</sup> and H<sup>+</sup>, forming PhCH<sub>2</sub>OOH with an adsorption structure

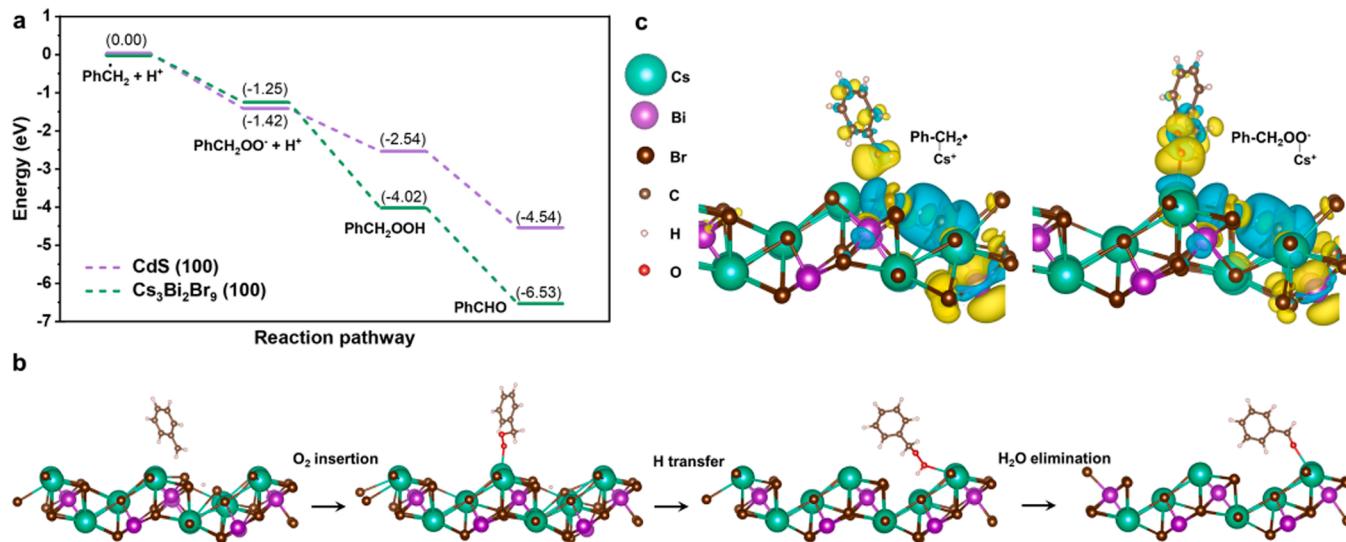


**Fig. 4.** (a) Reaction energy profiles of toluene oxidation (benzyl radical as the reactant) with oxygen under the surface of CdS (100) and Cs<sub>3</sub>Bi<sub>2</sub>Br<sub>9</sub> (100). (b) Structure evolutions of different key intermediates adsorbed on the surface of Cs<sub>3</sub>Bi<sub>2</sub>Br<sub>9</sub> (100) and their corresponding reaction processes. (c) The charge density difference maps of adsorbed intermediates (benzyl radical and peroxide anion) on the Cs<sub>3</sub>Bi<sub>2</sub>Br<sub>9</sub> (100) surface.

through another O-Cs bond (3.19 Å), in which the adsorbed O atom is in the carbonyl group instead of the terminal O atom in the O-O peroxy bond. Finally, the elimination of H<sub>2</sub>O from PhCH<sub>2</sub>OOH to generate PhCHO product.

Besides, charge density difference is also utilized to investigate the interaction between intermediates and the surface of Cs<sub>3</sub>Bi<sub>2</sub>Br<sub>9</sub> (100). As shown in Fig. 4c, negative electrons and positive charge tend to be distributed between C/O atoms of intermediates and Cs<sup>+</sup> of Cs<sub>3</sub>Bi<sub>2</sub>Br<sub>9</sub>, which further proves that the interaction between intermediate radicals and Cs<sub>3</sub>Bi<sub>2</sub>Br<sub>9</sub> (100) surface is primary through C-Cs or O-Cs bond. These results reveal that Cs<sup>+</sup> cations might play key roles in the surface activation for the conversion of aromatic C(sp<sup>3</sup>)-H bonds.

The surface reaction process on CdS (100) surface is similar and the interaction between intermediates and CdS surface is mainly via C-Cd or O-Cd bond (Figs. S24 and S25). The adsorption energy of intermediates on Cs<sub>3</sub>Bi<sub>2</sub>Br<sub>9</sub> or CdS surface is calculated, as shown in Fig. S26. A lower adsorption energy of the key intermediate facilitates the conversion on the Cs<sub>3</sub>Bi<sub>2</sub>Br<sub>9</sub> surface, since too strong interaction between intermediates and surface is not favourable for the surface transformations between adsorbed species. Besides, analysis of plane-averaged electron density difference of different transition states on Cs<sub>3</sub>Bi<sub>2</sub>Br<sub>9</sub> or CdS surface along Z axis (parallel with the adsorption bond) is also performed (Fig. S27). PhCH<sub>2</sub>· or PhCH<sub>2</sub>OO· on Cs<sub>3</sub>Bi<sub>2</sub>Br<sub>9</sub> (100) or CdS (100) surface, considering the significant difference for the adsorption energy. These results demonstrate that Cs<sub>3</sub>Bi<sub>2</sub>Br<sub>9</sub> has a smaller charge accumulation and electron density difference, showing weaker interactions with intermediates. It shows that there is lower charge accumulation where there is steric hindrance on Cs<sub>3</sub>Bi<sub>2</sub>Br<sub>9</sub> surface, which contributes to the faster surface transformations of intermediates. Results from the plane-averaged electron density difference analysis also match well with the adsorption energy which reveals the interaction between adsorbed species and surface, as well. All these analytical results might explain the difference of catalytic or activation effects between Cs<sub>3</sub>Bi<sub>2</sub>Br<sub>9</sub> and CdS. The weaker adsorption, larger space and less steric hindrance between intermediates and surfaces, might be more beneficial the conversion of reaction species.

### 3.6. Synergistic catalytic effects

The schematic illustration for the photo and surface synergistic catalysis for the aromatic C(sp<sup>3</sup>)-H conversion with oxygen is shown in Fig. 5, which consists of light-driven redox steps via energetic photo-induced e<sup>-</sup>/h<sup>+</sup> and the surface activation/catalysis processes on perovskite active sites, similar to the natural photosynthesis system including photo reactions and dark reactions.

The above results demonstrate the efficient catalytic effect of

Cs<sub>3</sub>Bi<sub>2</sub>Br<sub>9</sub> surface for the activation and conversion of key intermediates. During the surface catalysis, A/X (Cs/Br) site of halide perovskite derivative play key roles for different reaction steps, including the ·O<sub>2</sub> insertion, H<sup>+</sup> transfer and H<sub>2</sub>O elimination, which reveals that the unique surface properties of halide perovskite may possess catalytic effects for C(sp<sup>3</sup>)-H activation and even other photocatalytic reactions. It is well known that B and X sites dominate energy band structures in halide perovskite-based photocatalysts [73–75], which are considered as the functional components for the photocatalytic reaction processes. However, synergistic catalytic effects of A/X sites for the surface activation and reaction steps are important, as well, which should be given more attentions.

## 4. Conclusion

In summary, we demonstrated that surface activation and catalytic effects on the halide perovskite derivative also play a key role for promoting the photocatalytic conversion of aromatic C(sp<sup>3</sup>)-H bonds, combined with charge separation effects in the heterojunction. Active sites on halide surfaces in a new type of heterostructured photocatalyst, provides a more thermodynamically and kinetically favorable reaction pathway for the conversion of key intermediates. A wide variety of aromatic substrates can be effectively converted with high activity and selectivity. We believe that this study not only expands the scope of functional building blocks for the family of emerging halide perovskites and derivatives, but also provides a unique perspective for investigation of photocatalytic mechanism of halide perovskite and addresses the importance of considering the surface catalysis and reaction process while developing efficient and novel halide perovskite-based photocatalysts.

### CRediT authorship contribution statement

**Yalin Yang:** Conducting most of processes of the research and investigation, mainly for the synthesis of the photocatalysts, characterizations of materials and photocatalytic experiments. **Zheyang Chen:** Conducting a part of experiments and participating in the data analysis. **Hanlin Huang:** Responsible for the Conceptualization, Methodology, Verification of experimental results, data analysis, Data curation, Writing – original draft, Writing – review & editing, Supervision, Funding acquisition. **Yuxin Liu:** Completing the schemes of the manuscript. **Junhua Zou:** Providing assistance of the experimental characterizations of reaction products. **Shuqi Shen:** Conducting a part of the photocatalytic experiments. **Jiawei Yan:** Providing assistance of photoelectrical experiments. **Jinshui Zhang:** Providing methods for the analysis of reaction products. **Zanyong Zhuang:** Providing methods for

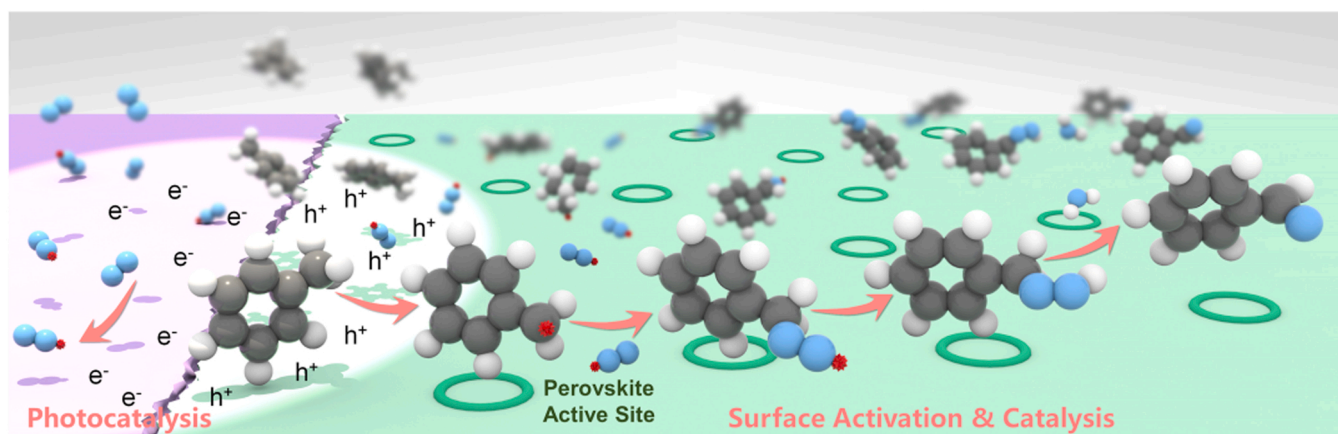


Fig. 5. Schematic illustration for the photocatalysis and synergistic surface activation effects and catalytic pathways for the aromatic C(sp<sup>3</sup>)-H conversion with oxygen, under light irradiation and during surface chemical reactions.



the photoelectrical experiments. **Zhongzhen Luo**: Participating in the data analysis. **Chenkai Yang**: Conducting the theoretical calculations. **Yan Yu** : Providing Supervision, Reviewing, Funding. **Zhigang Zou**: Providing Supervision, Reviewing, Funding, Experimental conditions.

## Declaration of Competing Interest

The authors declare that they have no known competing financial interests or personal relationships that could have appeared to influence the work reported in this paper.

## Data Availability

Data will be made available on request.

## Acknowledgements

This work was supported primarily by National Key Research and Development Program of China (2020YFA0710303), National Natural Science Foundation of China (No. 22109024, U1905215 and 52072076), Natural Science Foundation of Fujian Province of China (No. 2021J01595) and the Fujian Science and Technology Innovation Laboratory for Optoelectronic Information of China (2021ZZ127). We thank the Analytical Instrumentation Center of Fuzhou University for the assistance of in-situ XPS experiment and Prof. Chengkai Yang for the DFT calculations. We are grateful to Prof. Yan Yu and Prof. Zhigang Zou for the supervision of this work.

## Appendix A. Supporting information

Supplementary data associated with this article can be found in the online version at doi:10.1016/j.apcatb.2022.122146.

## References

- X. Qiu, Y. Zhang, Y. Zhu, C. Long, L. Su, S. Liu, Z. Tang, Applications of nanomaterials in asymmetric photocatalysis: Recent progress, challenges, and opportunities, *Adv. Mater.* 33 (2021) 2001731.
- L. Buzzetti, G.E.M. Crisenza, P. Melchiorre, Mechanistic studies in photocatalysis, *Angew. Chem. Int. Ed.* 58 (2019) 3730–3747.
- Y. Miao, Y. Zhao, S. Zhang, R. Shi, T. Zhang, Strain engineering: a boosting strategy for photocatalysis, *Adv. Mater.* (2022) 2200868.
- H. Tong, S. Ouyang, Y. Bi, N. Umezawa, M. Oshikiri, J. Ye, Nano-photocatalytic materials: possibilities and challenges, *Adv. Mater.* 24 (2012) 229–251.
- H. Yu, R. Shi, Y. Zhao, G.I.N. Waterhouse, L.-Z. Wu, C.-H. Tung, T. Zhang, Smart utilization of carbon dots in semiconductor photocatalysis, *Adv. Mater.* 28 (2016) 9454–9477.
- B. Samanta, Á. Morales-García, F. Illas, N. Goga, J.A. Anta, S. Calero, A. Bieberle-Hütter, F. Libisch, A.B. Muñoz-García, M. Pavone, M. Caspari Toroker, Challenges of modeling nanostructured materials for photocatalytic water splitting, *Chem. Soc. Rev.* 51 (2022) 3794–3818.
- Q. Guo, C. Zhou, Z. Ma, X. Yang, Fundamentals of TiO<sub>2</sub> photocatalysis: concepts, mechanisms, and challenges, *Adv. Mater.* 31 (2019) 1901997.
- J. Low, J. Yu, M. Jaroniec, S. Wageh, A.A. Al-Ghamdi, Heterojunction photocatalysts, *Adv. Mater.* 29 (2017) 1601694.
- P. Zhou, J. Yu, M. Jaroniec, All-solid-state Z-scheme photocatalytic systems, *Adv. Mater.* 26 (2014) 4920–4935.
- H. Li, W. Tu, Y. Zhou, Z. Zou, Z-scheme photocatalytic systems for promoting photocatalytic performance: recent progress and future challenges, *Adv. Sci.* 3 (2016) 1500389.
- L.-W. Zhang, Y.-J. Wang, H.-Y. Cheng, W.-Q. Yao, Y.-F. Zhu, Synthesis of porous Bi<sub>2</sub>WO<sub>6</sub> thin films as efficient visible-light-active photocatalysts, *Adv. Mater.* 21 (2009) 1286–1290.
- Y. Wang, P. Du, H. Pan, L. Fu, Y. Zhang, J. Chen, Y. Du, N. Tang, G. Liu, Increasing solar absorption of atomically thin 2D carbon nitride sheets for enhanced visible-light photocatalysis, *Adv. Mater.* 31 (2019) 1807540.
- J. Jian, Y. Xu, X. Yang, W. Liu, M. Fu, H. Yu, F. Xu, F. Feng, L. Jia, D. Friedrich, R. Van De Krol, H. Wang, Embedding laser generated nanocrystals in BiVO<sub>4</sub> photoanode for efficient photoelectrochemical water splitting, *Nat. Commun.* 10 (2019) 2609.
- C. Gao, Q. Meng, K. Zhao, H. Yin, D. Wang, J. Guo, S. Zhao, L. Chang, M. He, Q. Li, H. Zhao, X. Huang, Y. Gao, Z. Tang, Co<sub>3</sub>O<sub>4</sub> hexagonal platelets with controllable facets enabling highly efficient visible-light photocatalytic reduction of CO<sub>2</sub>, *Adv. Mater.* 28 (2016) 6485–6490.
- X. Xie, N. Zhang, Z.-R. Tang, M. Anpo, Y.-J. Xu, Ti<sub>3</sub>C<sub>2</sub>Ti<sub>x</sub> Mxene as a janus cocatalyst for concurrent promoted photoactivity and inhibited photocorrosion, *Appl. Catal. B Environ.* 237 (2018) 43–49.
- C.A. Walenta, C. Courtois, S.L. Kollmannsberger, M. Eder, M. Tschurl, U. Heiz, Surface species in photocatalytic methanol reforming on Pt/TiO<sub>2</sub>(110): Learning from surface science experiments for catalytically relevant conditions, *ACS Catal.* 10 (2020) 4080–4091.
- H. Huang, Y. Jina, Z. Chai, X. Gu, Y. Liang, Q. Li, H. Liu, H. Jiang, D. Xu, Surface charge-induced activation of Ni-loaded CdS for efficient and robust photocatalytic dehydrogenation of methanol, *Appl. Catal. B Environ.* 257 (2019), 117869.
- B. Qiu, M. Du, Y. Ma, Q. Zhu, M. Xing, J. Zhang, Integration of redox cocatalysts for artificial photosynthesis, *Energy Environ. Sci.* 14 (2021) 5260–5288.
- J. Yang, D. Wang, H. Han, C. Li, Roles of cocatalysts in photocatalysis and photoelectrocatalysis, *Acc. Chem. Res.* 46 (2013) 1900–1909.
- R. Croce, H. van Amerongen, Natural strategies for photosynthetic light harvesting, *Nat. Chem. Biol.* 10 (2014) 492–501.
- B. Saparov, D.B. Mitzi, Organic-inorganic perovskites: structural versatility for functional materials design, *Chem. Rev.* 116 (2016) 4558–4596.
- H. Huang, M.I. Bodnarchuk, S.V. Kershaw, M.V. Kovalenko, A.L. Rogach, Lead halide perovskite nanocrystals in the research spotlight: Stability and defect tolerance, *ACS Energy Lett.* 2 (2017) 2071–2083.
- M.V. Kovalenko, L. Protesescu, M.I. Bodnarchuk, Properties and potential optoelectronic applications of lead halide perovskite nanocrystals, *Science* 358 (2017) 745–750.
- Z. Shi, J. Guo, Y. Chen, Q. Li, Y. Pan, H. Zhang, Y. Xia, W. Huang, Lead-free organic-inorganic hybrid perovskites for photovoltaic applications: Recent advances and perspectives, *Adv. Mater.* 29 (2017) 1605005.
- Y. Tang, C.H. Mak, G. Jia, K.-C. Cheng, J.-J. Kai, C.-W. Hsieh, F. Meng, W. Niu, F.-F. Li, H.-H. Shen, X. Zhu, H.M. Chen, H.-Y. Hsu, Lead-free hybrid perovskite photocatalysts: Surface engineering, charge-carrier behaviors, and solar-driven applications, *J. Mater. Chem. A* 10 (2022) 12296–12316.
- H. Mai, D. Chen, Y. Tachibana, H. Suzuki, R. Abe, R.A. Caruso, Developing sustainable, high-performance perovskites in photocatalysis: Design strategies and applications, *Chem. Soc. Rev.* 50 (2021) 13692–13729.
- W. Wang, M.O. Tade, Z. Shao, Research progress of perovskite materials in photocatalysis- and photovoltaics-related energy conversion and environmental treatment, *Chem. Soc. Rev.* 44 (2015) 5371–5408.
- S. Pan, J. Li, Z. Wen, R. Lu, Q. Zhang, H. Jin, L. Zhang, Y. Chen, S. Wang, Halide perovskite materials for photo(electro)chemical applications: Dimensionality, heterojunction, and performance, *Adv. Energy Mater.* (2021) 2004002.
- N. Glück, T. Bein, Prospects of lead-free perovskite-inspired materials for photovoltaic applications, *Energy Environ. Sci.* 13 (2020) 4691–4716.
- Z. Zhang, Y. Liang, H. Huang, X. Liu, Q. Li, L. Chen, D. Xu, Stable and highly efficient photocatalysis with lead-free double-perovskite of Cs<sub>2</sub>AgBiBr<sub>6</sub>, *Angew. Chem. Int. Ed.* 58 (2019) 7263–7267.
- H. Lei, D. Hardy, F. Gao, Lead-free double perovskite Cs<sub>2</sub>AgBiBr<sub>6</sub>: fundamentals, applications, and perspectives, *Adv. Funct. Mater.* 31 (2021) 2105898.
- G. Chen, P. Wang, Y. Wu, Q. Zhang, Q. Wu, Z. Wang, Z. Zheng, Y. Liu, Y. Dai, B. Huang, Lead-free halide perovskite Cs<sub>3</sub>Bi<sub>2</sub>Sb<sub>2</sub>Cl<sub>9</sub> (X approximately 0.3) possessing the photocatalytic activity for hydrogen evolution comparable to that of (CH<sub>3</sub>NH<sub>3</sub>)PbI<sub>3</sub>, *Adv. Mater.* 32 (2020) 2001344.
- S.S. Bhosale, A.K. Kharade, E. Jokar, A. Fathi, S.-M. Chang, E.W.-G. Diao, Mechanism of photocatalytic CO<sub>2</sub> reduction by bismuth-based perovskite nanocrystals at the gas-solid interface, *J. Am. Chem. Soc.* 141 (2019) 20434–20442.
- L. Romani, A. Speltini, C.N. Dibenedetto, A. Listorti, F. Ambrosio, E. Mosconi, A. Simbula, M. Saba, A. Profumo, P. Quadrelli, F.D. Angelis, L. Malavasi, Experimental strategy and mechanistic view to boost the photocatalytic activity of Cs<sub>3</sub>Bi<sub>2</sub>Br<sub>9</sub> lead-free perovskite derivative by g-C<sub>3</sub>N<sub>4</sub>, *Adv. Funct. Mater.* 32 (2021) 2104428.
- M.V. Kovalenko, L. Protesescu, M.I. Bodnarchuk, Properties and potential optoelectronic applications of lead halide perovskite nanocrystals, *Science* 358 (2017) 745–750.
- Z.-L. Liu, R.-R. Liu, Y.-F. Mu, Y.-X. Feng, G.-X. Dong, M. Zhang, T.-B. Lu, In situ construction of lead-free perovskite direct Z-scheme heterojunction Cs<sub>3</sub>Bi<sub>2</sub>I<sub>9</sub>/Bi<sub>2</sub>WO<sub>6</sub> for efficient photocatalysis of CO<sub>2</sub> reduction, *Sol. Rrl.* 5 (2021) 2000691.
- X.D. Wang, Y.H. Huang, J.F. Liao, Y. Jiang, L. Zhou, X.Y. Zhang, H.Y. Chen, D. B. Kuang, In situ construction of a Cs<sub>2</sub>SnI<sub>6</sub> perovskite nanocrystal/SnS<sub>2</sub> nanosheet heterojunction with boosted interfacial charge transfer, *J. Am. Chem. Soc.* 141 (2019) 13434–13441.
- T. Wang, D. Yue, X. Li, Y. Zhao, Lead-free double perovskite Cs<sub>2</sub>AgBiBr<sub>6</sub>/rGO composite for efficient visible light photocatalytic H<sub>2</sub> evolution, *Appl. Catal. B Environ.* 268 (2020), 118399.
- Y. Zhu, Y. Liu, Q. Ai, G. Gao, L. Yuan, Q. Fang, X. Tian, X. Zhang, E. Egan, P. M. Ajayan, J. Lou, In situ synthesis of lead-free halide perovskite-COF nanocomposites as photocatalysts for photoinduced polymerization in both organic and aqueous phases, *ACS Mater. Lett.* 4 (2022) 464–471.
- H. Huang, D. Verhaeghe, B. Weng, B. Ghosh, H. Zhang, J. Hofkens, J.A. Steele, M.B. J. Roeffaers, Metal halide perovskite-based heterojunction photocatalysts, *Angew. Chem. Int. Ed.* 61 (2022) 202203261.
- L. Wang, H. Xiao, T. Cheng, Y. Li, W.A. Goddard, Pb-activated amine-assisted photocatalytic hydrogen evolution reaction on organic-inorganic perovskites, *J. Am. Chem. Soc.* 140 (2018) 1994–1997.
- W.-J. Yin, B. Weng, J. Ge, Q. Sun, Z. Li, Y. Yan, Oxide perovskites, double perovskites and derivatives for electrocatalysis, photocatalysis, and photovoltaics, *Energy Environ. Sci.* 12 (2019) 442–462.

- [43] Q. Ji, L. Bi, J. Zhang, H. Cao, X.S. Zhao, The role of oxygen vacancies of ABO<sub>3</sub> perovskite oxides in the oxygen reduction reaction, *Energy Environ. Sci.* 13 (2020) 1408–1428.
- [44] R. Mandal, B. Garai, B. Sundararaju, Weak-coordination in C-H bond functionalizations catalyzed by 3D metals, *ACS Catal.* 12 (2022) 3452–3506.
- [45] X. Meng, X. Cui, N.P. Rajan, L. Yu, D. Deng, X. Bao, Direct methane conversion under mild condition by thermo-, electro-, or photocatalysis, *Chem* 5 (2019) 2296–2325.
- [46] D. Balcells, E. Clot, O. Eisenstein, C-H bond activation in transition metal species from a computational perspective, *Chem. Rev.* 110 (2010) 749–823.
- [47] G. Kresse, J. Furthmüller, Efficiency of ab-initio total energy calculations for metals and semiconductors using a plane-wave basis set, *Comput. Mater. Sci.* 6 (1996) 15–50.
- [48] G. Kresse, J. Furthmüller, Efficient iterative schemes for ab initio total-energy calculations using a plane-wave basis set, *Phys. Rev. B* 54 (1996) 11169.
- [49] Y. Dai, C. Poidevin, C. Ochoa-Hernández, A.A. Auer, H. Tüysüz, A supported bismuth halide perovskite photocatalyst for selective aliphatic and aromatic C-H bond activation, *Angew. Chem. Int. Ed.* 59 (2020) 5788–5796.
- [50] Q. Li, T. Song, Y. Zhang, Q. Wang, Y. Yang, Boosting photocatalytic activity and stability of lead-free Cs<sub>3</sub>Bi<sub>2</sub>Br<sub>9</sub> perovskite nanocrystals via in situ growth on monolayer 2D Ti<sub>3</sub>C<sub>2</sub>T<sub>x</sub> MXene for C-H bond oxidation, *ACS Appl. Mater. Inter.* 13 (2021) 27323–27333.
- [51] Z. Zhang, Y. Yang, Y. Wang, L. Yang, Q. Li, L. Chen, D. Xu, Revealing the A-site effect of lead-free A<sub>3</sub>Sb<sub>2</sub>Br<sub>9</sub> perovskite in photocatalytic C(sp<sup>3</sup>)-H bond activation, *Angew. Chem. Int. Ed.* 59 (2020) 18136–18139.
- [52] H. Huang, H. Yuan, J. Zhao, G. Solís-Fernández, C. Zhou, J.W. Seo, J. Hendrix, E. Debroye, J.A. Steele, J. Hofkens, J. Long, M.B.J. Roelfaers, C(sp<sup>3</sup>)-H bond activation by perovskite solar photocatalyst cell, *ACS Energy Lett.* 4 (2019) 203–208.
- [53] Y. Zhao, Y. Dai, Q. Wang, Y. Dong, T. Song, A. Mudryi, Q. Chen, Y. Li, Anions-exchange-induced efficient carrier transport at CsPbBr<sub>3</sub>Cl<sub>3-x</sub>/TiO<sub>2</sub> interface for photocatalytic activation of C(sp<sup>3</sup>)-H bond in toluene oxidation, *ChemCatChem* 13 (2021) 1–8.
- [54] Z.-J. Bai, X.-P. Tan, L. Chen, B. Hu, Y.-X. Tan, Y. Mao, S. Shen, J.-K. Guo, C.-T. Au, Z.-W. Liang, S.-F. Yin, Efficient photocatalytic toluene selective oxidation over Cs<sub>3</sub>Bi<sub>1.8</sub>Sb<sub>0.2</sub>Br<sub>9</sub> nanosheets: Enhanced charge carriers generation and C-H bond dissociation, *Chem. Eng. Sci.* 247 (2022), 116983.
- [55] Z.-J. Bai, Y. Mao, B.-H. Wang, L. Chen, S. Tian, B. Hu, Y.-J. Li, C.-T. Au, S.-F. Yin, Tuning photocatalytic performance of Cs<sub>3</sub>Bi<sub>2</sub>Br<sub>9</sub> perovskite by g-C<sub>3</sub>N<sub>4</sub> for C(sp<sup>3</sup>)-H bond activation, *Nano Res.* (2022), <https://doi.org/10.1007/s12274-022-4835-z>.
- [56] J. Song, C. Zhang, H. Zhang, D. Dai, Q. Zhang, Z. Wang, Z. Zheng, Y. Liu, H. Cheng, Y. Dai, B. Huang, P. Wang, In situ growth of lead-free perovskite Cs<sub>2</sub>AgBiBr<sub>6</sub> on a flexible ultrathin carbon nitride sheet for highly efficient photocatalytic benzylic C(sp<sup>3</sup>)-H bond activation, *Chem. Eng. Sci.* 453 (2023), 139748.
- [57] Y.H. Park, I. Jeong, S. Bae, H.J. Son, P. Lee, J. Lee, C.-H. Lee, M.J. Ko, Inorganic rubidium cation as an enhancer for photovoltaic performance and moisture stability of HC(NH<sub>2</sub>)<sub>2</sub>PbI<sub>3</sub> perovskite solar cells, *Adv. Funct. Mater.* 27 (2017) 1605988.
- [58] G. Xing, M.H. Kumar, W.K. Chong, X. Liu, Y. Cai, H. Ding, M. Asta, M. Grätzel, S. Mhaisalkar, N. Mathews, T.C. Sum, Solution-processed Tin-based perovskite for near-infrared lasing, *Adv. Mater.* 28 (2016) 8191–8196.
- [59] M.S. Chen, M.C. White, Combined effects on selectivity in Fe-catalyzed methylene oxidation, *Science* 327 (2010) 566–571.
- [60] S. Xie, Z. Shen, J. Deng, P. Guo, Q. Zhang, H. Zhang, C. Ma, Z. Jiang, J. Cheng, D. Deng, Y. Wang, Visible light-driven C-H activation and C-C coupling of methanol into ethylene glycol, *Nat. Commun.* 9 (2018) 1181.
- [61] X. Lang, J. Zhao, Integrating TEMPO and its analogues with visible-light photocatalysis, *Chem. - Asian J.* 13 (2018) 599–613.
- [62] L. Zhang, J. Zhang, H. Yu, J. Yu, Emerging S-scheme photocatalyst, *Adv. Mater.* 34 (2022) 2107668.
- [63] H. Huang, D. Verhaeghe, B. Weng, B. Ghosh, H. Zhang, J. Hofkens, J.A. Steele, M.B. J. Roelfaers, Metal halide perovskite based heterojunction photocatalysts, *Angew. Chem. Int. Ed.* 61 (2022), e202203261.
- [64] Q. Xu, L. Zhang, B. Cheng, J. Fan, J. Yu, S-scheme heterojunction photocatalyst, *Chem* 6 (2020) 1543–1559.
- [65] M. Shi, G. Li, W. Tian, S. Jin, X. Tao, Y. Jiang, E.A. Pidko, R. Li, C. Li, Understanding the effect of crystalline structural transformation for lead-free inorganic halide perovskites, *Adv. Mater.* 32 (2020) 2002137.
- [66] S. Guan, X. Fu, Y. Zhang, Z. Peng, Beta-NiS modified CdS nanowires for photocatalytic H<sub>2</sub> evolution with exceptionally high efficiency, *Chem. Sci.* 9 (2018) 1574–1585.
- [67] S. Kumar, I. Hassan, M. Regue, S. Gonzalez-Carrero, E. Rattner, M.A. Isaacs, S. Eslava, Mechanochemically synthesized Pb-free halide perovskite-based Cs<sub>2</sub>AgBiBr<sub>6</sub>-Cu-rGO nanocomposite for photocatalytic CO<sub>2</sub> Reduct., *J. Mater. Chem. A* 9 (2021) 12179–12187.
- [68] K. Ohkubo, K. Suga, K. Morikawa, S. Fukuzumi, Selective oxygenation of ring-substituted toluenes with electron-donating and with drawing substituents by molecular oxygen via photoinduced electron transfer, *J. Am. Chem. Soc.* 125 (2003) 12850–12859.
- [69] A. Ishikawa, T. Takata, J.N. Kondo, M. Hara, H. Kobayashi, K. Domen, Oxsulfide Sm<sub>2</sub>Ti<sub>2</sub>S<sub>2</sub>O<sub>5</sub> as a stable photocatalyst for water oxidation and reduction under visible light irradiation (λ ≤ 650 nm), *J. Am. Chem. Soc.* 124 (2002) 13547–13553.
- [70] Y.-F. Xu, X.-D. Wang, J.-F. Liao, B.-X. Chen, H.-Y. Chen, D.-B. Kuang, Amorphous-TiO<sub>2</sub>-encapsulated CsPbBr<sub>3</sub> nanocrystal composite photocatalyst with enhanced charge separation and CO<sub>2</sub> fixation, *Adv. Mater. Interfaces* 5 (2018) 1801015.
- [71] L. Wang, H. Xiao, T. Cheng, Y. Li, W.A. Goddard, Pb-activated amine-assisted photocatalytic hydrogen evolution reaction on organic-inorganic perovskites, *J. Am. Chem. Soc.* 140 (2018) 1994–1997.
- [72] B. Maillard, K.U. Ingold, J.C. Scaiano, Rate constants for the reactions of free radicals with oxygen in solution, *J. Am. Chem. Soc.* 105 (1983) 5095–5099.
- [73] Q. Fan, G.V. Biesold-McGee, J. Peng, Z. Lin, J. Ma, Q. Xu, S. Pan, Lead-free halide perovskite nanocrystals: crystal structures, synthesis, stabilities, and optical properties, *Angew. Chem. Int. Ed.* 59 (2020) 1030–1046.
- [74] M.V. Kovalenko, L. Protesescu, M.I. Bodnarchuk, Properties and potential optoelectronic applications of lead halide perovskite nanocrystals, *Science* 358 (2017) 745–750.
- [75] T. He, Y. Jiang, X. Xing, M. Yuan, Structured perovskite light absorbers for efficient and stable photovoltaics, *Adv. Mater.* 32 (2020) 1903937.